

Sea-ice permittivity derived from GNSS reflection profiles: Results of the MOSAiC expedition

A. Maximilian Semmling, Jens Wickert, Frederik Kress, M. Mainul Hoque,
Dmitry V. Divine, Sebastian Gerland, Gunnar Spreen

Abstract

Reflectometry measurements have been conducted aboard the German research icebreaker *Polarstern* during the MOSAiC expedition (Multidisciplinary drifting Observatory for the Study of Arctic Climate). Signals of Global Navigation Satellite Systems (GNSS) were recorded using a dedicated GNSS reflectometry receiver for retrieval of sea-ice reflectivity. The primary goal is a reflectometry-based monitoring of sea ice as part of the Arctic climate study. The data set presented here covers the expedition's first leg (late Sep. to mid Dec. 2019) in the Siberian Sector of the central Arctic (at about 82°N to 87°N). Daily profiles of reflectivity are retrieved for satellite elevations $< 45^\circ$. In agreement with model prediction the results show best reflectivity contrast (about 5 dB between compact pack-ice and lower ice concentrations) for observations at left-handed circular polarization and elevation angles of 10° to 20°. A daily resolved time series of sea-ice relative permittivity is inverted from the left-handed data. In general, the level of inversion results is at the lower limit of sea-ice values (rel. permittivity of 3 and below), potentially indicating an influence of incoherent volume scattering. Occasional increase of relative permittivity is attributed to the presence of water. Sea-ice profiles show anomalies that are confirmed by enhanced model prediction (slab reflection). A long-term comparison of prediction and retrieved profiles indicates anomalies' dependence on ice thickness and temperature.

A. M. Semmling and M. M. Hoque are with German Aerospace Center DLR, Institute for Solar-Terrestrial Physics, Neustrelitz, Germany, e-mail: maximilian.semmling@dlr.de.

J. Wickert and F. Kress are with German Research Centre for Geosciences GFZ and with Technische Universität Berlin, Germany.

D. Divine and S. Gerland are with Norwegian Polar Institute, Fram Centre, Tromsø, Norway.

G. Spreen is with University of Bremen, Institute of Environmental Physics, Bremen, Germany.

Index Terms

Sea-ice Permittivity, Reflectometry, Satellite Navigation Systems, MOSAiC Expedition.

I. INTRODUCTION

Sea ice is an important factor in the Earth's energy budget affecting ocean and atmosphere. The albedo of an ice-covered ocean is higher than the albedo of open water. It means that absorption of solar energy at the Earth's surface is lower for ice-covered areas. Monitoring of the Arctic and Antarctic sea-ice cover is, therefore, an essential contribution to the global energy budget and climate models. As a consequence of global warming the ice extent in the Arctic has significantly decreased over the last decades, especially in summer [1]. A unique opportunity to study Arctic sea ice arises from the MOSAiC project (Multidisciplinary drifting Observatory for the Study of Arctic Climate), see, for example, [2], [3] and [4]. Core of the project is an expedition of the German research icebreaker *Polarstern* [5]. The corresponding cruise to the central Arctic lasted from September 2019 until October 2020. During the expedition the ship was drifting for more than nine months with the Arctic sea ice.

This paper refers to reflectometry measurements conducted aboard *Polarstern* using signals of Global Navigation Satellite Systems (GNSS). The major objective of the here presented study is to understand the impact of changing sea-ice conditions on GNSS reflectometry observations and to reveal new opportunities for ice property retrievals. The measurements covered the entire period of the ship's year-long ice drift. Here, data from the first leg (September to December 2019) of the freezing period are considered.

Sea ice exhibits pronounced seasonal variations. The ice forms mainly in the autumn/winter period and usually melts from late spring to late summer. Accordingly, the extent of Arctic sea ice is largest in early spring and smallest in late summer. The so-called aging process between formation and melting changes the physical ice properties and defines the concept of ice types. Sea ice that started to form after the last summer melting period and experienced not more than one winter's growth is called first-year ice. The persistence of sea-ice cover in the central Arctic after the melting period can extend the aging period over multiple years resulting in so-called multiyear ice. Sea ice that survived one summer melt is called second-year. The ice types can differ significantly in thickness, salinity and roughness, cf. [6], [7]. Based on values in the given literature we will use the term first-year (FY) and multiyear (MY) to discriminate the ice types of different salinity.

Sea-ice extent and concentration can be monitored on a global scale using scanning-mode microwave radiometers [8]. Also GNSS reflectometry algorithms provide scatterometric products to determine sea-ice extent [9], [10] or they contribute to radiometer observations [11]. New findings on reflectometry-based retrievals of sea-ice parameter can foster application as proposed, for example, in the G-TERN mission concept [12].

Current remote sensing techniques for ice thickness retrieval involves altimetric and radiometric approaches [13], [14]. Altimeter observations from Cryosat-2 are used for thick ice (> 1 m) on weekly basis. Radiometric retrievals improve the performance for thinner ice (< 1 m), e.g., based on SMOS (Soil Moisture & Ocean Salinity) satellite data with a daily resolution. The interpretation of radiometric measurements over sea ice is complex. Apart from thickness the measurement also depends on other sea-ice properties, like salinity, temperature or snow cover. The sea-ice permittivity, as a key quantity for radiometric techniques, is ambiguous under changes of temperature and salinity. The permittivity is also a limiting factor of signal penetration into sea ice. A fact that is used in microwave radiometry for thickness retrieval, cf. [15]. Further impact on permittivity and signal penetration will arise from the inhomogeneity of sea ice (changing temperature across the ice and variable snow thickness on top).

The primary goal of this study is the estimation of sea-ice relative permittivity using data recorded during MOSAiC (first leg). Similar estimates have been reported earlier by [16] based on aircraft measurements. This earlier study provided a solution to the fundamental problem of separating permittivity and roughness response in the GNSS data. Open questions remained like the impact of upper and lower interface reflection (air-ice and ice-water) on the response. This question is essential for ice thickness retrievals. Recent work on satellite data, [17] and [18], examined retrievals of sea-ice height and thickness, respectively. Both studies give indication that the lower (ice-water) interface is dominating the reflection response of sea ice. Ground-based measurements, also performed during MOSAiC with a reflectometry setup directly on the ice, demonstrated the retrieval of sea-ice thickness and revealed the impact of the snow cover on reflection signatures [4].

A secondary goal is to clarify the impact of ice interfaces: upper (air-ice) and lower (ice-water), on the observed reflectivity. The reflectometry data from *Polarstern* and predictions of dedicated reflectivity models will be examined. In a first model approach a bulk sea-ice medium is assumed, cf. [16]. A second approach considers a slab reflection model including contributions from the lower interface [15].

The paper is structured in seven sections. This introduction part is followed by section II on the experimental setting and reflectometry measurements (MOSAIC expedition's first leg). The third section describes the signal processing to reach reflectivity estimates. Then section IV examines the two models of sea-ice reflection and gives predicted reflectivity profiles at different compositions of the sea-ice system. Results of reflectivity retrieval and permittivity inversion are presented in section V. The discussion of the results including anomalies in the observed reflectivity profiles can be found in section VI. The last part is dedicated to conclusions and outlook.

II. EXPERIMENTAL SETTING AND MEASUREMENTS

The first leg of the expedition started on 20-Sep-2019 from Tromsø, Norway (69.65°N, 18.95°E). During a 10-days transit *Polarstern* went from there to the Siberian sector of the Arctic. After another 4-days search and reconnaissance in the ice the ship was moored to the designated floe on 4-Oct [2] and started the drift (in-ice period). The here analyzed reflectometry data set begins during the transit on 28-Sep (DoY 271) and ends with the expedition's first leg in the central Arctic on 14-Dec (DoY 348), cf. map in Fig. 1.

So the data set consists of a short part in the late transit period (DoY 271 to 273) and a long part in the in-ice period (DoY 273 to 348). No observations are available during the early transit through the Exclusive Economic Zones of Norway and Russia in late September. The here-described GNSS setup included also a geodetic receiver that provided data for long-term monitoring of atmospheric water vapor in the Arctic [19].

A. Sea Ice Parameter and Ship Velocity

Ancillary data is gathered in Fig. 1 to characterize the in-ice and late transit period. Panel (b) shows 2-m air temperature and sea-ice temperature assumed for a 1.0-to-1.5 m deep ice layer, both parameters are derived from ERA-5 reanalysis products (available via <https://cds.climate.copernicus.eu>). This panel also gives the ice thickness d_{sat} along the ship trajectory, based on daily SMOS data before 15-Oct (DoY 288) and afterwards on the weekly combined SMOS/CryoSat-2 product from AWI (both available via <https://data.meereisportal.de>). Early SMOS-based thickness data during the in-ice period can be compared with in-situ measurements d_{sit} from the distributed network around the ship [2]. On 7-Oct values of 44 cm and 67 ± 54 cm are obtained for d_{sat} and

d_{sit} , respectively. Similar results are reported for 5-Oct and 9-Oct. The comparison indicates a significant variability of ice thickness in the 40-km radius around the ship.

Panel (c) of Fig. 1 shows estimates of sea-ice types and corresponding partial ice concentrations, given by visual observations from the ship's bridge using the ASSIST observation protocol [20]. Panel (d), finally, contains the ship's velocity (daily mean and standard deviation) in horizontal and vertical components v_h and v_v . These data are retrieved from the GORS receiver's GPS Doppler observations. The difference in v_h between transit and in-ice period is obvious. The ship was moored to the dedicated ice floe on 4-Oct (DoY 277) that later became a core of the Arctic observatory, cf. [2]. After mooring the daily mean of v_h is below 0.5 m/s, i.e., significantly smaller than the ship's common cruising speed in open water of 5 m/s. Changes of v_h are then induced by the drifting ice. Corresponding patterns might be related to the inner ice dynamics.

B. Reflectometry Measurements

Instrumentation for reflectometry comprised a GORS type receiver (GNSS Occultation Reflectometry Scatterometry) equipped with three antenna links: the master link of an up-looking antenna and two slave links of a side-looking antenna. The receiver is able to apply master-slave tracking for GPS C/A and GPS L2C signals at L1 and L2 carrier frequencies, respectively. More details on the receiver board (later version) are found at "<https://www.javad.com/jgnss/products/oem/Quattro-R/specifications.html>". Similar master-slave measurements with this receiver type have been described in [21] and [22]. The two slave links allow a dual-polarization record: with right-handed and left-handed circular polarization (RHCP and LHCP). The master link is implemented using a JAVAD GrAnt G3T patch antenna with a 5 dB peak gain and a 3 dB-beamwidth of 110°. For the slave links a dual-polarization patch antenna 3G1215RL-PP-XS-X from ANTCOM is used with 4.7 dB peak gain and a 3 dB-beamwidth of 114°. The antennas were mounted with a small baseline (length < 20 cm) on the port side of the ship's observation deck at a height h_a of about 21 m above water level. Reflections of GPS signals were recorded in an elevation range between 1° and 45°. This range and the given height h_a define specular reflection points on the sea surface in a distance from the ship's port side between 1 200 m and 20 m, respectively. A scheme of the reflectometry concept is shown in Fig. 2.

III. SIGNAL PROCESSING

Internally the GORS receiver uses a lock-loop algorithm to track the direct signal received on the master link in code delay, Doppler frequency and carrier phase. The slave links are sampled in an open-loop tracking relative to the master, cf. airborne experiments [21], [23]. The here-presented measurements in the drift experiment have rather short relative delay range between reflected and direct signals, shorter than the C/A code correlation range (about 300 m), and small respective Doppler shifts (< 1 Hz). It implies on the one hand that a delay or Doppler correction of the slave open-loop tracking relative to the master is not required. It also implies that direct and reflected signals overlap and show respective contribution in both master and slave samples. The receiver provides in-phase and quadrature (post-correlation) samples for the master and slave links with 5 ms coherent integration (at 200 Hz). The following study concentrates on the L1 C/A signal record.

A. Signal Power from Slave Samples

In a first post-processing step direct and reflected signals' contribution are separated within the slave samples. The small baseline between master and slave antennas allow to identify the direct signal as long-period (small Doppler shift) signatures in the slave samples. A second-order polynomial fit over 2-minute segments is used to find these direct signal contributions. Signatures of sea-surface reflection in the master and slave samples have significant shorter periods (larger Doppler shifts). The reason is that for the given setup the antennas' height (about 21 m above the reflecting surface) is considerably larger than the baseline between the antennas (about 20 cm). The reflection signatures are resolved by computing a series of Lomb-Scargle periodograms (LSP) over 2-minute segments using the in-phase and quadrature samples. For LSP computation a variable transformation (time to sine of elevation angle) is performed on the sample time-series. This transformation implies that the frequency scale changes to a height scale in the LSP. Procedure and benefit of LSP computation for near-surface reflectometry are described in [24]. Examples of fitting and LSP computation to separate direct and reflected contributions in the ship-borne case can be found in a previous study [25].

In a second step power profiles over elevation angle are estimated. The 2-minute segment average of the fitted in-phase, quadrature components $\overline{I_d}$, $\overline{Q_d}$ leads to the direct power estimate $P_d = \overline{I_d}^2 + \overline{Q_d}^2$. The estimates are then stacked and normalized in 1-deg elevation bins resulting in direct power profiles $P_d(E)$ over the 1° to 45° range. Also the series of LSP are stacked

and normalized in 1-deg elevation bins keeping height resolution. In this way height-elevation maps of power $P(h, E)$ are produced. The stacking of LSP to the final maps emphasizes main reflection contributions. For the two slave links $P(h, E)$ maps are shown in panels (a) and (b) of Fig. 3.

The given examples refer to the first day of the in-ice period (DoY 273) when the ship was still cruising. Stacking includes all observations of the respective day. Signal power estimates of the first leg, as a result of these processing steps, can be found in the following data publication [26]. Due to height mapping of LSP we clearly see in $P(h, E)$ that peak reflection power occur at $h_a \approx 21$ m in agreement with the antenna height level relative to the sea surface. Accordingly, elevation profiles of the sea-surface reflection power follow by fixing the height $P_r(h_a, E)$. The sea-surface reflection (at h_a) clearly dominates the shown maps of daily stacking. Potentially, all nearby multipath reflections can influence these maps. The broadening of the sea-surface signature beyond 30° might be related to the increasing role of ship multipath. By fixing the height $h = h_a$ for the profile, the sea-surface reflection is extracted. Other multipath contributions that would usually appear at different heights are mitigated in the profiles. Further mitigation of multipath was not performed.

In addition to direct and reflected power also noise level is estimated. It is computed from the variance of quadrature samples in the master and lies typically between 60 and 70 dB. Power estimates are significantly above noise level, cf. panel (c) in Fig. 3.

B. Reflectivity from Power Estimates

Based on power profiles, described above, the reflectivity is derived. We use the direct power profile of the RHCP slave link, here denoted $P_1(E)$, as reference for reflectivity computation. The reflected power profiles of the LHCP, RHCP slave links are denoted $P_2(E)$, $P_3(E)$, respectively. The cross- and co-polar ratios are formed

$$\begin{aligned} p_{\text{cross}} &= P_2/P_1, \\ p_{\text{co}} &= P_3/P_1. \end{aligned} \tag{1}$$

These ratios are assumed to present surface reflectivity r at cross- and co-polarization of the GNSS signal. All three estimates P_1 , P_2 and P_3 refer to the slave antenna with boresight pointing to the horizon. In this way two effects are mitigated: the gain pattern (same gain for

direct and specularly reflected signals due to symmetrical incidence) and the gain control (three slave front-ends are attached to one dual-polarization slave antenna). Furthermore variations of the free-space path loss cancel in the ratio of reflected and direct power as the path length difference is considerable smaller than the individual path lengths. Residual uncertainties of power (ratio) estimates are discussed in section VI.

IV. REFLECTIVITY MODELS AND PREDICTION

Under consideration of uncertainties, discussed later, the ratios in eq.(1) yield estimates of reflectivity r . Based on the derivation in [25] the reflectivity can be modeled by $r = |R|^2 |S|^2$ where R is the reflection coefficient and S is the loss induced by surface roughness. In a first approach a reflection at a smooth interface of two bulk media shall be considered, disregarding roughness.

A. Bulk Reflection Model

The reflection coefficients for an interface of air with a bulk sea-ice medium are given, parallel and perpendicular to the incidence plane, by

$$\begin{aligned} R_{\parallel} &= \frac{\epsilon_{\text{ice}} \sin E - \sqrt{\epsilon_{\text{air}} \epsilon_{\text{ice}} - (\epsilon_{\text{air}} \cos E)^2}}{\epsilon_{\text{ice}} \sin E + \sqrt{\epsilon_{\text{air}} \epsilon_{\text{ice}} - (\epsilon_{\text{air}} \cos E)^2}} \\ R_{\perp} &= \frac{\epsilon_{\text{air}} \sin E - \sqrt{\epsilon_{\text{air}} \epsilon_{\text{ice}} - (\epsilon_{\text{air}} \cos E)^2}}{\epsilon_{\text{air}} \sin E + \sqrt{\epsilon_{\text{air}} \epsilon_{\text{ice}} - (\epsilon_{\text{air}} \cos E)^2}}. \end{aligned} \quad (2)$$

They involve the elevation angle E and the relative permittivity ϵ_{air} , ϵ_{ice} of respective media. The here given form, with R_{\parallel} and R_{\perp} , further relates to a co- and cross-polar form $R^{\text{co}} = (1/2) (R_{\parallel} + R_{\perp})$ and $R^{\text{cross}} = (1/2) (R_{\parallel} - R_{\perp})$. An ideal GNSS signal is assumed reaching the receiver with RHCP on the direct path. Then reflectivity, in co- and cross-polar form, is given by the ratios specified in eq.(1). The additional effect of roughness can be considered by adding the loss factor

$$S = \exp\left(\frac{1}{2} \left(\frac{2\pi}{\lambda}\right)^2 (\delta h \sin E)^2\right) \quad (3)$$

in the reflectivity model r . It depends on the standard deviation of surface height δh , as roughness parameter, and again on the elevation angle E . The first approach of a bulk reflection model cannot cover other aspects of sea-ice reflection. It disregards underlying water and accumulated snow (above the ice).

B. Slab Reflection Model

We refer to the dielectric slab of ice on the water surface as given in [15]. The model states a reflection coefficient R combining contributions from the upper interface (air-ice) with a reflection coefficient R_1 and the lower interface (ice-water) with R_2 . Here, we denote the combined solution R_{aiw} indicating the involved media (air, ice, water) and the respective coefficients at interfaces R_{ai} and R_{iw} assuming bulk reflections, according to eq.(2). The combined solution reads

$$R_{\text{aiw}} = \frac{R_{\text{ai}} + R_{\text{iw}} e^{-2ik_{\text{ice},z}d}}{1 + R_{\text{ai}} R_{\text{iw}} e^{-2ik_{\text{ice},z}d}}, \quad (4)$$

with dependencies $R_{\text{ai}}(E_{\text{air}}, \epsilon_{\text{air}}, \epsilon_{\text{ice}})$ and $R_{\text{iw}}(E_{\text{ice}}, \epsilon_{\text{ice}}, \epsilon_{\text{water}})$ where relative permittivity ϵ of the respective media and the corresponding elevation angles E are considered. Furthermore, it involves the slab thickness parameter d . The thickness impact is modulated by a phase constant β_{ice} and an attenuation coefficient α_{ice} . They relate to the wave vector's z-component $k_{\text{ice},z} = \beta_{\text{ice}} - i\alpha_{\text{ice}}$ and are defined as

$$\begin{aligned} \alpha_{\text{ice}} &= \frac{2\pi}{\lambda} \cos E_{\text{ice}} \text{Im} \{ \sqrt{\epsilon_{\text{ice}}} \} \\ \beta_{\text{ice}} &= \frac{2\pi}{\lambda} \cos E_{\text{ice}} \text{Re} \{ \sqrt{\epsilon_{\text{ice}}} \} \end{aligned} \quad (5)$$

where λ is the L-band carrier wavelength, E_{ice} is the elevation angle above the lower (ice-water) interface that corresponds to the refraction angle and ϵ_{ice} denotes the relative permittivity of the ice slab, here, carrying two properties: the refractivity and the conductivity given by the real and imaginary parts of $\sqrt{\epsilon}$, respectively.

Comparing bulk and slab reflection models, the number of independent parameters increases from one (ϵ_{ice}) to three (d , as well as the real and imaginary part of ϵ_{ice}). We assume here that relative permittivity of air above and sea water below are known apriori.

Based on the sea-ice slab model we can study the effect of underlying water. The effect of accumulated snow requires to include another layer and a corresponding multi-layer model extension. In agreement with the approach in [4] we iterate the slab-reflection model, based on eq.(4). Then the reflection coefficient assuming air (upper bulk medium), snow (upper layer), sea ice (lower layer) and water (lower bulk medium) reads

medium	(1) air	(2) water 2°C	(3) FY ice −1°C −10°C	(4) MY ice −1°C −10°C	(5) dry snow 0.1 g cm ^{−3}
real part of ϵ	1	76.4	4.75 4.21	3.31 3.24	1.16
imag. part of ϵ	-	48.5	0.91 0.62	0.11 0.07	-

TABLE I
CONSIDERED MEDIA AND RESPECTIVE PERMITTIVITY VALUES.

$$\begin{aligned}
 R_{\text{asiw}} &= \frac{R_{\text{as}} + R_{\text{siw}} e^{-2ik_{\text{snow},z}d}}{1 + R_{\text{as}} R_{\text{siw}} e^{-2ik_{\text{snow},z}d}} \\
 R_{\text{siw}} &= \frac{R_{\text{si}} + R_{\text{iw}} e^{-2ik_{\text{ice},z}d}}{1 + R_{\text{si}} R_{\text{iw}} e^{-2ik_{\text{ice},z}d}}.
 \end{aligned} \tag{6}$$

with dependencies as stated before. Two difficulties arise for the multi-layer extension: the number of ancillary input parameters further increases and the assumption of a layered structure is questioned by the dynamic sea-ice conditions we face in the long-term ship-borne measurements. We will use the extended model only to predict the tendency of dry snow affecting the sea-ice slab reflection and leave a higher complexity of different snow types and depths for future studies. Further studies may also profit from early work on GNSS reflectometry over soil [27] where a multi-layer model has been described that also includes roughness effects.

C. Predicted Reflectivity

Table I defines the L-band relative permittivity of respective media used in this study.

Air (1) is taken at vacuum limit. The sea water values (2) are typical for polar oceans at a temperature of 2°C and a salinity of 34.0 psu, cf. [28]. Winter temperature might be slightly lower with negligible effect on ϵ . For sea ice two different types are considered: first-year ice (3) and multiyear ice (4). The corresponding ice parameter are: salinity of 4.0 psu for FY, 0.5 psu for MY and temperature as specified in the table. The sea-ice values are computed with brine volume and L-band specific parameters given in [29] and [15], respectively. Additionally, lossless dry snow (5) is considered according to [30] for the given density. Exchange of snow with brine (salt water in sea ice) or sea water is disregarded.

Fig. 4 shows predictions of co- and cross-polar reflectivity considering bulk and slab reflection under different configurations.

Considering the bulk model, as reference, the co-polar profile shows a characteristic fall over elevation whereas the cross-polar profile is rising, cf. respective red curves in Fig. 4. The bulk model also predicts that changing media with a lowering of permittivity (e.g. going from water to ice) results in an increase of r_{co} and a decrease of r_{cross} , cf. relation of respective solid and dashed red curves. This response of r_{cross} to ϵ is confirmed by previous studies [31], [25]. However, these studies also indicated that observations of r_{co} do not confirm, or even contradict, the model. This point of deviation between model and observation in the co-polar (RHCP) case is also found in soil-moisture related reflectometry studies. An early observation study [24] reported the increase of RHCP reflection amplitude with increase of permittivity (water content). Expectation from model side is different, the co-polar reflection coefficient slightly increases when soil permittivity (water content) decreases, cf. [32].

D. Anomaly of Sea-ice Profiles

The use of a bulk model to describe sea-ice reflection assumes that the penetration depth into the ice is smaller than its thickness. Otherwise contributions from the lower ice-water interface will occur. The slab reflection model, as an extension of the bulk model, shall overcome the assumption and reveal slab anomalies induced by the ice-water interface. There is no significant difference of bulk and slab ice model results for r_{co} , cf. dashed curves in panels (a) and (b) of Fig. 4. Obvious differences occur for r_{cross} depending on the slab medium conductivity $\text{Im}\{\epsilon\}$, cf. Tab. I. Ice types with rather high conductivity (FY salinity) do not show slab anomalies unless the slab is thin enough (here 0.1 m), see panel (e) in Fig. 4. For larger slab thickness there is no anomaly and the FY profiles agree with the bulk model.

The slab anomaly becomes clearer for lower conductivity (MY salinity). Fluctuations of the profiles arise from coherent superposition of upper and lower interface contribution (air-ice and ice-water), see panel (d) and (f) in Fig. 4. A shorter fluctuation period relates to a larger thickness, see the oscillatory part $\exp -2i\beta d$ in eq.(4).

An important step is to quantify the slab anomaly. We focus on the signature in the low-elevation range (E_{low} from 3° to 10°) where coherence of reflection is usually preserved. A reference bulk profile r_{cross} has a steep slope in this range. The respective slope of MY slab profiles is significantly different. The mean gradients $\langle dp/dE \rangle|_{E_{low}}$ are 1.0, 0.4 and -0.1 dB/ $^\circ$ for bulk ice, 1 m- and 0.1 m-slabs, respectively. Here, the 0.1 m-slab value has only theoretical meaning as Arctic MY ice is larger in thickness.

E. Snow Layer Effect

Another important question is how profiles, concentrating on cross-polar ones, are affected by accumulated snow. The multi-layer extension of the slab reflection model, cf. eq.(6), can help in this respect. Profiles for snow/ice layers on top of bulk water are shown in panel (c) and (d) of Fig. 4 (black dotted curves). The considered dry snow (DS) has a negligible conductivity and is penetrated by the signal. The FY ice layer, in panel (c), is not penetrated. Here, the anomaly is purely induced by the snow layer. In the MY case the ice anomaly is additionally modulated by the snow effect. In general, the dry snow affects the slope in a similar way as low-conductivity ice. The gradient $\langle dp/dE \rangle|_{E_{\text{low}}}$ with $0.1 \text{ dB}/^\circ$ is significantly smaller than the bulk value. At low elevations the snow-affected profile lies above the ice-slab profile. At higher elevation angles the snow-affected profiles tend to be below. The reflectivity level at mid elevations (20°) does not change drastically. These findings are based on the dry-snow assumption. Even under cold conditions an exchange of brine and sea water with the snow layer may occur that alters the snow properties.

V. RESULTS OF REFLECTIVITY RETRIEVAL AND PERMITTIVITY INVERSION

Power ratios p_{cross} , p_{co} are computed, with daily resolution, for the entire leg-1 data set. The conditions differ significantly between the late transit period (Sep, DoY 271-273) and the late in-ice period (Dec, DoY 335-348). The late transit period has rather high temperatures (air above -10°C) and is still influenced by open water (SIC usually $< 90\%$). The late in-ice period has permanently compact ice (total SIC 100%) and a low temperature (air below -15°C), cf. Fig. 1. During the in-ice period the primary ice type (second-year) remains constant, as the ship is moored (starboard) to the selected floe of this type. In the antenna field of view (port side) the ice changed occasionally. There, cracks with new ice growth and drifting ice relative to the ship were observed.

A. Retrieved Reflectivity

Retrieved profiles p_{cross} and p_{co} for the two different periods are plotted in Fig. 5.

Results of the late-transit period (high permittivity, water-dominated) and in-ice period (low permittivity, ice-dominated) are compared. The predicted decrease of r_{cross} , going from a water- to an ice-dominated surface, is confirmed. By contrast, the corresponding increase of r_{co} in this case is not found. The behavior of p_{co} is opposite and indicates that the current model for r_{co} is

not suitable for an inversion of ϵ using the co-polar ratio. We concentrate on cross-polar ratios p_{cross} in the following analysis.

The three transit profiles p_{cross} in upper-right panel of Fig. 5, are in rather good agreement with the bulk medium predictions (solid and dashed red curves) for low-range elevations. The reflectivity level, in general, is lower than bulk water prediction indicating the presence of sea ice, cf. SIC in Fig. 1. From mid-range elevations on, $> 10^\circ$, an additional roughness effect appears that can be modeled (dotted red curve) based on eq.(3).

The p_{cross} profiles of the late in-ice period, lower right panel in Fig. 5, clearly differ from the ones of the transit period in the upper panel. The in-ice results have local minimum at about 10° whereas the transit results show a local maximum there. The level at mid-range elevation (10° to 20°) is lower for the in-ice results, a roughness effect as before is not detected. The turn from local maximum to minimum yields an slope anomaly at low elevations, $E_{\text{low}} : < 10^\circ$. The rising slope turns to mainly falling slope, cf. upper right to lower right panels. Based on the predicted anomalies, above, we interpret the changing slope as an indication of a compact sea-ice layer reflection with contribution of the ice-water interface.

The anomaly is quantified for all profiles by a linear fit of p in the E_{low} range. Additionally, we apply a linear fit for mid-range elevations (E_{mid} defined between 10° and 30°), cf. black fitting lines in Fig. 5. From the fitting lines $\tilde{p} = m E + n$ in the respective ranges, indicated by $_{\text{low}}$ and $_{\text{mid}}$, we retrieve a mid-range power ratio estimate at 20° of elevation and a low-range slope estimate

$$\tilde{p}_{\text{mid}}(E = 20^\circ) \quad \text{and} \quad m_{\text{low}} \quad (7)$$

The mid-range estimate \tilde{p}_{mid} allows us to obtain the reflectivity level while mitigating both: the low-range slab anomaly and the increasing roughness effect at higher elevation angles. In the mid range the inversion of relative permittivity ϵ based on the bulk reflection model, cf. eq. (2), is most promising. The monotonic bulk model function of reflectivity at the given elevation $r_{\text{blk}}(\epsilon, E = 20^\circ)$ is easily inverted

$$\tilde{\epsilon} = \epsilon(r_{\text{blk}} = \tilde{p}_{\text{mid}})|_{E=20^\circ} \cdot \quad (8)$$

B. Inverted Permittivity

Results $\tilde{\epsilon}$ from the available leg-1 data (28-Sep to 14-Dec) are shown in Fig. 6.

Cross-polar estimates $\tilde{\epsilon}$, in the upper panel, are found in a typical range for sea-ice and snow relative permittivity, between 1 and 6. Co-polar estimates, by contrast, are not in a reasonable range. The poor performance of the co-polar model to describe the reflection power and corresponding inversion of ϵ has already been reported before, cf. discussion of Fig. 4 and the previous studies mentioned there. A model improvement in this point shall be considered for future studies. The cross-polar results will be further analyzed here.

The ice floe, the ship is drifting with, is classified as second-year ice [2], cf. Fig. 1. The salinity of this ice is, by now, not explicitly known to the authors. It will be available in future when ice cores taken from the floes are fully analyzed. From on-site observation it is clear that the ice had significant spatial variability with a high fraction of refrozen melt ponds imbedded into older second-year ice and frequent ridges. On average a low salinity of the second-year ice, more comparable to multiyear ice than to first-year ice, is expected due to drainage of brine that has occurred during the summer months.

The cross-polar results in Fig. 6 show a low level of permittivity (2 to 3) over long periods. It indicates a low salinity of the encountered ice in agreement with our expectation for second-year ice. However, the overall sea-ice permittivity seems to be underestimated by the results as the permittivity of second-year ice is to be expected above the MY value of about 3.

VI. DISCUSSION

A. Incoherent Scattering and Coherent Signatures

For long periods in Fig. 6 the level of relative permittivity estimates is low. The median of all estimates is 2.4, so below the MY value ($|\epsilon|$ of about 3) which is regarded as the lower limit for sea-ice. The overall minimum 1.8 on DoY 285 is close to the dry-snow value, cf. Tab. I. However, the low level cannot be explained by the presence of a dry-snow. The multi-layer model (sea-ice and dry-snow layers) does not indicate a significant decrease of reflectivity due to snow in the considered elevation range (at about 20°), cf. Fig. 4 (c) and (d).

Incoherent scattering might be an explanation. It is induced by inhomogenities of the ice with a scale of the signal wavelength or larger that prevent coherent reflection (according to the slab model). This scattering will reduce the coherent reflection power and is likely to increase with

elevation angle [°]	30	20	10	1
major axis ¹ [m]	6 (2)	11 (4)	31 (6)	609 (99)
minor axis ¹ [m]	3 (1)	3 (1)	5 (1)	15 (5)
roughness limit ² [cm]	< 10	< 10	10	140
distance of spec. point ³ [m]	36 (3)	58 (5)	119 (11)	1197 (115)

TABLE II

REFLECTION PARAMETER WITH IMPACT ON COHERENCE, ¹ AXES OF 1ST FRESNEL ZONE, ² LIMIT δh ACCORDING TO RAYLEIGH CRITERION, ³ ON SPHERICAL EARTH SURFACE. AN ANTENNA HEIGHT OF 21 M (2 M) ABOVE THE SURFACE IS ASSUMED.

elevation angle. Anomalies of the slab model, as the oscillations predicted in Fig. 4 (c) to (f), are expected to disappear due to incoherent scattering.

The previous study within MOSAiC [4] showed coherent signatures involving ice and snow reflection also at high elevations (30° and above). The fraction of coherent reflection, reported there, can be assumed to be higher due to a smaller sensor height (about 2 m compared to about 21 m of the setup here). The reason is the smaller footprint of the 2 m-high sensor that covers less inhomogeneties (scatterers) affecting coherence.

Two reflection parameters are analyzed to better understand the loss of coherence and the onset of incoherent scattering. One parameter is the size of the first Fresnel zone. This zone defines the surface area that contributes to a coherent reflection. Inhomogeneties of the ice that fall within this zone will certainly affect coherence. The other parameter is roughness given by the vertical variations δh of the surface that will limit coherent reflection according to the Rayleigh criterion [33]. Table II shows the evolution of these parameters over the relevant elevation angles.

A critical roughness limit < 10 cm is stated for high and mid-range elevations (> 10°). The ice vertical variability can exceed this limit taking into account the standard variation of 54 cm that was reported for in-situ sea-ice thickness measurements [2]. The limit becomes considerably less critical at lowest elevations (< 10°) when roughness of up to 1.4 m (at 1°) can be tolerated. The footprint size stretches, in particular on the major axis, towards lowest elevations. A significant reduction of footprint size is reported when reducing the antenna height from 21 to 2 m.

The applied stacking of power estimates (from different tracks) will further enlarge the footprint. Depending on the elevation considered for the estimation, permittivity at 20° and anomaly below 10°, a footprint circle around the ship has to be considered with a radius of

69 m or > 150 m, respectively. Here, the radius is the sum of spec. point distance and major axis, cf. values in Tab. II. For ship-based measurements a further increase of footprint can be expected due to the distance traveled over the stacking time. Here, however, we can assume that the footprint on-ice stays constant as the ship drifts with the ice. It has to be mentioned that the given footprint estimate does not include all potential scatterers. As shown recently [34], scatterers that exceed in dimensions the 1st Fresnel zone have impact on the reflected power, in particular, if they are offset from the specular point. In the sea-ice scenario, ridges that rise from the level ice could be such scatterers.

We can conclude that dominance of coherent conditions is not likely to happen. Conditions differ across elevations. The probability of coherent condition increases at lowest elevation angles. Therefore, specific elevation ranges were selected: mid-range for the permittivity estimation and low-range for slab anomaly retrieval, cf. definitions in eq.(7).

B. Ice Breaking Events

Apart from the generally low level of cross-polar estimates $\tilde{\epsilon}$ in Fig. 6 there are three obvious clusters of higher estimates. The first one (C1) is still in the travel period starting with DoY 271, a second one (C2) between DoY 295 and 299 and the third (C3) starting with DoY 321. We know from panel (c) of Fig. 1 that ice type changes in the drift period (for C2 and C3) are rare. Only occasionally cracks and new ice appeared port side. The primary ice type (second-year) did not change. Cluster C1 is obviously before the drift started when water was still present (total SIC $< 100\%$). Cluster C2 follows a period of younger ice reported in the secondary ice type from DoY 290 to 295. The cluster C3 coincides with a storm event starting on DoY 320 that led to ice breaking and opening of a crack with open water/thin ice next to the ship. A part of the on-ice measurements had to be stopped during this storm [4].

Areas of open water may form close to the ship by inner ice stress, by wind and ocean currents or by the cruising ship breaking the ice. The occurrence of both, sea ice at low permittivity and a share of water at high permittivity, results in the intermediate (mixing) value estimated during these clusters. The impact of water can be used to estimate sea-ice concentration as shown in a previous study [25].

The hypothesis that estimates $\tilde{\epsilon}$ are increased due to ice breaking is strengthened by a comparison with the ship's velocity data in Fig. 1. The clusters (C1, C2, C3) coincide with epochs of significantly increased horizontal velocity reported for DoY 271 to 277 (travel period), for

DoY 294 to 297 and for DoY 320 to 322 (storm event). We interpret that the increased velocity is accompanied by ice breaking and lead formation. Ice breaking can be either actively by the ship, as for the large velocity range on the early four days when the ship was still searching for an ice floe, or by other factors, like wind, that result in ice break-ups and lead formation close to the ship during the in-ice period.

The high-value clusters and respective changes in the velocity also coincide with rather high values of air temperature, cf. again Fig. 1. The total temperature range of this period is between -4°C in Oct. and -26°C in Nov./Dec. The cluster occur at about -9°C , -12°C and -10°C , respectively. The higher temperatures indicate warmer air masses advected towards MOSAiC, which are associated to cyclones with higher wind speeds and wind gradients. These in turn can cause stress to be build up in the ice, which is released when ice drift gets more divergent.

C. Anomalies and Sea-ice Impact

Based on the predicted reflectivity in Fig. 4 anomalies in the observed profiles can be related to slab reflection. Corresponding fluctuations occur if slab thickness and conductivity are small enough (limited loss) to allow contributions from the slab's lower interface. It is expected that the slope in the low elevation range of the reflectivity profile m_{low} changes significantly between bulk and slab reflection. The slope retrievals, from the entire in-ice data set, and slope predictions, from the slab model $r(d, \epsilon)$, are derived. Linear fits are used as indicated in Fig. 5. Predictions and retrievals are shown in Fig. 7.

The predictions of m_{low} in panel (a) show the slope as a function of slab thickness d . Only the cross-polar case is shown as the predicted effect in the co-polar case is insignificant. The slope fluctuates with increasing d . For ice with rather high conductivity (FY) the fluctuations quickly saturate at the typical value of bulk reflection $m_{\text{low}} \approx 1.2 \text{ dB}/^{\circ}$. For low conductivity ice (MY) the fluctuations extend to d of 2 m and more. Ice at low temperature is further reduced in conductivity, cf. imaginary part of ϵ in Tab. I. It leads to a further extension of corresponding fluctuations towards greater thicknesses, cf. red and blue dotted curves in panel (a) of Fig. 7. All three curves, for FY, MY at -1°C and MY at -10°C , reach asymptotically, for large d , the bulk reflection limit $m_{\text{low}} \approx 1.2 \text{ dB}/^{\circ}$. The slope value of a thin MY slab, up to 100 cm, is significantly below the bulk limit. It means that we can identify slabs, with contributions of the lower slab interface, by small slope values $m_{\text{low}} < 1 \text{ dB}/^{\circ}$.

The model prediction shows resonance peaks in the fluctuations. Overall minima of m_{low} occur at 90 cm (130 cm) and maxima at 110 cm (200 cm) for a MY slab at -1°C (-10°C). The lower temperature (-10°C) induces a shift of slope characteristics towards greater slab thickness.

Panels (b),(c) of Fig. 7 present the retrievals for co- and cross-polar data and predictions assuming the three ice types of panel (a). Slab thickness for the prediction is modeled using the ancillary ice thickness data, cf. panel (b) of Fig. 1, keeping in mind the larger footprint of the satellite products.

Predictions of the co-polar case, panel (b), are not sensitive to ice type changes, all types have a slope of about $-0.4\text{ dB}/^{\circ}$. The corresponding co-polar retrievals contrast the prediction. The retrieved slope changes considerable, it is usually above the prediction with a persistent anomaly of rising slopes (values > 0) in the late period. Predictions of the cross-polar case, panel (c), shows significant differences between the three ice types. The FY prediction reaches a saturated level (bulk limit) for the given thickness. The MY prediction shows fluctuations with changing amplitude and period (red and blue dotted curves). Between DoY 276 to about 290 the prediction is in good agreement with the retrievals. For the later period the two curves separate: the red curve (-1°C) approaches the bulk limit, whereas the blue curve (-10°C) further fluctuates at the lower level in better agreement with the retrievals.

The increasing ice thickness, assumed for the model during the observation period, causes increasing fluctuations in the MY predictions. Also retrievals show a tendency towards increasing fluctuation amplitude. It indicates that retrievals of the slope parameter m_{low} are sensitive to sea-ice thickness. With increasing thickness the temperature (conductivity) of the ice starts to play a role, as can be seen from the difference of red and blue curves. Obviously, the MY prediction curve for -10°C (blue one) fits the retrievals better than the curve for -1°C (red one). It indicates that also a sensitivity to ice temperature exists. The reader should keep in mind that model prediction is based on the assumption of a homogeneous ice slab. In reality sea ice is inhomogeneous with significant variations, e.g., in ice thickness over the observed footprint area and in temperature from upper to lower ice interface. Furthermore, accumulated snow will additionally affect the profile and has to be considered to interpret anomalies. The agreement of observed and predicted fluctuations will, therefore, be limited.

D. Polarization and Power Uncertainties

The mismatch of model prediction and observations for the co-polar ratio causes the respective estimation of ϵ to fail, see lower panel of Fig. 6. Earlier studies already indicated this mismatch, as discussed in relation to Fig. 4, above. A possible reason of this mismatch can be a crosstalk of the LHCP signal component in the RHCP antenna link. Such a crosstalk can lead the cross-polar behavior (increase of reflectivity for increasing permittivity) to dominate also in observations of the RHCP link as the co-polar dependence on permittivity is weaker, cf. Fig. 4.

In general, a bias of power estimates can be induced by the antenna gain pattern that varies for the here applied hemispherical patch antennas with incidence angle from about 4.7 dB in boresight direction to about -2.0 dB at the edge (90° off-boresight). The described processing assumes the antenna gain effect to cancel when computing the power ratios between reflected and direct signals. This assumption relies on the direct and reflected rays that reach the antenna with the same incidence angle relative to the antenna's boresight direction, here pointing to the horizon. Further variation in azimuth is not reported for the manufacturer's gain pattern.

In general, the processing does not consider the relative bearing of satellites. Observations are stacked resolving only the satellite elevation. A reason is the drift of the ship-based setup. The heading direction, that is needed to compute the relative bearing of satellites, cannot be derived from a single GNSS data set. The GNSS velocity vector that usually provides good estimates of the heading fails in this drift scenario when velocity vector and bow direction of the ship are considerably different. It is assumed that stacking itself serves as a filter to amplify the sea-surface reflection signature in boresight direction.

A part of the leg-1 data set (December events, DoY 335 to 348) is processed without stacking to assess the impact of stacking. Additional GNSS data of another receiver on the ship is available for this period. So the heading for the bearing computation can be obtained from the baseline between the two setups. Of course, also other sensor data can be used in future to correct the heading of the drifting ship. The distribution of power estimates over the satellite bearing relative to the ship's bow is shown for the given period in Fig. 8.

All panels of this figure show that observations are most frequent port-side, bearing of about -90° to -60° relative to the bow (0°). It is in agreement with the port-side location of the setup and with the orientation of the slave antenna (the unrestricted view to the sky and the sea surface port-side considering elevations $< 45^\circ$). The majority of all power estimates in (a), (b) and (d)

	(a) master link	(b) slave link*	(c) master noise	(d) slave link**
peak power [dB]	107	105	65	93
stacked power [dB]	105	102	65	89
bias of stacking [dB]	-2	-3	0	-4

TABLE III
COMPARISON OF POWER DISTRIBUTION AND STACKING RESULTS

is significantly above the noise level given in (c). The gain effect of the port-side pointing slave antenna is visible in the direct (b) and reflected (d) power estimates. We conclude that the gain pattern bias is mitigated when using the ratio of the two slave links.

An uncertainty arises from stacking as differences due to relative bearing are not resolved. The red markers in Fig. 8 indicate the result after stacking all plotted observations. The stack results and the peak value of the shown distribution are provided along with the relative bias in Tab. III.

Stacking in this assessment yields an underestimation of direct and reflected power with respect to the distribution peak. The bias magnitude for the reflected signal is by 1 dB higher than respective direct signal on the slave link. We conclude that stacking gives a good approximation of the peak power without further gain correction. The remaining bias may cause an underestimation of reflectivity (and permittivity) in the stacking-based retrieval. A small bias of reflectivity (-0.47 dB at 20° elevation for the given setup) results from the delay shift of the reflected signals correlation peak relative to delay of slave samples (here, equal to master). For cross-polar values this bias translate to a rel. permittivity change below 0.5, in the typical sea-ice range, and is disregarded.

VII. CONCLUSIONS AND OUTLOOK

The results show that the given Arctic scenario of the MOSAiC expedition allows GNSS reflectometry-based estimates of relative permittivity ϵ over sea ice. They also indicate that water occurrence (lead and open-water areas in the ice pack) and incoherent scatter of the ice are potential sources of bias. The successful estimation is based on cross-polar reflectivity profiles derived from the dedicated GORS four-frontend reflectometry receiver. Cross-polar profiles p_{cross} are obtained from the ratio of reflected and direct signal power using the LHCP and RHCP link,

respectively. Co-polar profiles obtained by the respective RHCP to RHCP ratio do not agree with the reflectivity model under the given conditions.

The study considers a bulk and a slab reflection model. The first one describes reflection at a single interface (air-ice) and disregards signal penetration. The second one describes a coherent superposition of contributions from two interfaces (air-ice and ice-water). The retrieved profiles p_{cross} show anomalies of slab reflection with respect to the bulk reference at low elevation angles ($< 10^\circ$). In contrast to previous findings [18], there is no indication that contribution of the upper interface (air-ice) can be disregarded. A multi-layer model (including accumulated snow), with interfaces: air-snow, snow-ice and ice-water, can be achieved by iterating the slab model. However, even the complex multi-layer model cannot explain the slight underestimation of ϵ compared to typical sea-ice values. Incoherent scatter of inhomogeneties (roughness) in the ice structure, that is not covered by layer models, play certainly a role.

For inversion of ϵ the bulk model is applied and the reflectivity is estimated at 20° elevation. The bulk model at a pre-defined elevation with a single parameter ϵ is easily inverted. The retrieval in mid-elevation range (at 20°) mitigates the bias of slab anomaly (present particularly in the low-elevation range) and the roughness-induced effects (being more important at higher elevations).

The cross-polar results of inversion are found in the sea-ice and snow range of ϵ between 1.2 and 6. Discrete peaks of increased ϵ can be explained by the appearance of open water in the field-of-view, e.g., when SIC drops below 100%. In addition to incoherent scatter the slight underestimation of ϵ is also related to the bias of the applied stacking algorithm.

An option for further sea-ice classification results from analyzing the slope m_{low} of cross-polar profiles in the low elevation range. The anomalies of slab reflection, that appear clearly in this range, can be quantified by m_{low} . The comparison with model predictions of m_{low} , adjusted in slab thickness and conductivity (cf. Fig. 7) shows a sensitivity of observations in this respect. Thin or low-conductivity ice has a slab anomaly with small values of m_{low} close to zero. Whereas ice with higher conductivity reaches the typical bulk reflection value of about $1.2 \text{ dB}/^\circ$, e.g. 0.5 m-thick first-year ice. For the in-ice period a coarse classification based on m_{low} and ancillary thickness data can be made. It indicates MY ice with low conductivity at low temperature (-10°C) which agrees quite well with the second-year ice type reported in ancillary observations.

We conclude that the permittivity of the sea-ice covered surface can be estimated from GNSS-

based reflectivity profiles. A further retrieval of sea-ice concentration, as a main parameter for the sea surface permittivity, is feasible, cf. [25]. The described retrieval of permittivity and of slab reflection anomalies may help to resolve the ice type (salinity) and other parameters (temperature, thickness). A solution of respective ambiguities in the reflectivity profiles is important and could be reached in combination with other sensors, e.g. radiometers. Further in-situ data of the MOSAiC expedition (sea-ice and snow parameter) are expected soon and will help to clarify the impact of snow on the derived reflectivity. Once data availability has increased a future study will extend from the expedition's first leg (2.5 months) to the other legs (another 7 months in the ice) to broaden the scope on seasonal and regional differences in the central Arctic and the marginal ice zone.

We note that the concept of permittivity retrieval may also apply to land surface applications (snow melt and soil moisture monitoring). An overall challenge is to apply the findings to satellite observations when profiling the reflection over elevation angle is not possible.

ACKNOWLEDGMENT

Data used in this manuscript were derived as part of MOSAiC (international Multidisciplinary drifting Observatory for the Study of the Arctic Climate), expedition tag MOSAiC20192020 (Project ID AWI_PS122_0). Essential support on setup and logistics came from Sylvia Magnussen, Thomas Gerber, Markus Ramatschi and GFZ's workshop in the Geodesy Department. Crew and science team of Polarstern, AWI and MOSAiC are gratefully acknowledged for running this great project. Special thanks to Gunnar Spreen for coordinating the MOSAiC remote sensing group and to the other data contributors: Lars Kaleschke, Robert Ricker and Aikaterini Tavri who supervised the measurements during the expedition. The GNSS measurements were realized in the ArGID project (Arctic GNSS Ice Detection) funded by GFZ. Additional on-board GNSS data for heading computation were provided by Martin Kriegel from IMPC Neustrelitz. The signal power estimates, used here, have been published [26]. Contributions to the manuscript work by DD and SG are partly funded through the Research Council of Norway project HAVOC [280292].

REFERENCES

- [1] J. Stroeve and D. Notz, "Changing state of Arctic sea ice across all seasons," *Environ. Res. Lett.*, vol. 13, p. 103001, 2018.
- [2] T. Krumpen, F. Birrien, F. Kauker, T. Rackow, L. von Albedyll *et al.*, "The MOSAiC ice floe: sediment-laden survivor from the Siberian shelf," *The Cryosphere*, vol. 14, pp. 2173–2187, 2020.

- [3] C. Katlein, V. Mohrholz, I. Sheikin, P. Itkin, D. V. Divine *et al.*, “Platelet Ice Under Arctic Pack Ice in Winter,” *Geophys. Res. Lett.*, 2020.
- [4] J. F. Munoz-Martin, A. Perez, A. Camps, S. Ribó, E. Cardellach *et al.*, “Snow and Ice Thickness Retrievals Using GNSS-R: Preliminary Results of the MOSAiC Experiment,” *Remote Sensing*, vol. 12, p. 4038, 2020.
- [5] Alfred-Wegener-Institut Helmholtz-Zentrum für Polar- und Meeresforschung, “Polar Research and Supply Vessel POLARSTERN Operated by the Alfred-Wegener-Institute,” *Journal of large-scale research facilities*, vol. 3, p. A119, 2017.
- [6] G. F. N. Cox and W. F. Weeks, “Salinity Variations in Sea Ice,” *Journal of Glaciology*, vol. 13, pp. 109–120, 1974.
- [7] W. B. Tucker, A. Gow, and W. F. Weeks, “Physical Properties of Summer Sea Ice in the Fram Strait,” *J. Geophys. Res.*, vol. 92, pp. 6787–6803, 1987.
- [8] G. Spreen, L. Kaleschke, and G. Heygster, “Sea ice remote sensing using AMSR-E 89-GHz channels,” *J. Geophys. Res.*, vol. 113, p. C02S03, 2008.
- [9] A. Alonso-Arroyo, V. U. Zavorotny, and A. Camps, “Sea Ice Detection Using U.K. TDS-1 GNSS-R Data,” *IEEE Trans. Geosci. Remote Sens.*, vol. 55, pp. 4989–5001, 2017.
- [10] Y. Zhu, T. Tao, K. Yu, X. Qu, S. Li, J. Wickert, and M. Semmling, “Machine Learning-Aided Sea Ice Monitoring Using Feature Sequences Extracted from Spaceborne GNSS-Reflectometry Data,” *Remote Sensing*, vol. 12, p. 3751, 2020.
- [11] D. Llaveria, J. F. Munoz-Martin, C. Herbert, M. Pablos, H. Park, and A. Camps, “Sea Ice Concentration and Sea Ice Extent Mapping with L-Band Microwave Radiometry and GNSS-R Data from the FFSCat Mission Using Neural Networks,” *Remote Sens.*, vol. 13, 2021.
- [12] E. Cardellach, J. Wickert, and al., “GNSS Transpolar Earth Reflectometry exploriNg System (G-TERN): Mission Concept,” *IEEE Access*, vol. 6, pp. 13 980–14 018, 2018.
- [13] L. Kaleschke, X. Tian-Kunze, N. Maaß, A. Beitsch, A. Wernecke *et al.*, “SMOS sea ice product: Operational application and validation in the Barents Sea marginal ice zone,” *Remote Sensing of Environment*, vol. 180, pp. 264–273, 2016.
- [14] R. Ricker, S. Hendricks, L. Kaleschke, X. Tian-Kunze, J. King, and C. Haas, “A weekly Arctic sea-ice thickness data record from merged CryoSat-2 and SMOS satellite data,” *The Cryosphere*, vol. 11, pp. 1607–1623, 2017.
- [15] L. Kaleschke, N. Maaß, C. Haas, S. Hendricks, G. Heygster, and R. T. Tonboe, “A sea-ice thickness retrieval model for 1.4 GHz radiometry and application to airborne measurements over low salinity sea-ice,” *The Cryosphere*, vol. 4, pp. 583–592, 2010.
- [16] M. Belmonte Rivas, J. A. Maslanik, and P. Axelrad, “Bistatic Scattering of GPS Signals Off Arctic Sea Ice,” *IEEE Geosci. Remote Sens.*, vol. 48, no. 3, pp. 1548–1553, 2010.
- [17] W. Li, E. Cardellach, F. Fabra, A. Rius, S. Ribó, and M. Martín-Neira, “First Spaceborne Phase Altimetry over Sea Ice Using TechDemoSat-1 GNSS-R Signals,” *Geophys. Res. Lett.*, vol. 44, pp. 8369–8376, 2017.
- [18] Q. Yan and W. Huang, “Sea Ice Thickness Measurement Using Spaceborne GNSS-R: First Results With TechDemoSat-1 Data,” *IEEE JSTAR*, vol. 13, pp. 577–587, 2020.
- [19] B. Männel, F. Zus, G. Dick, S. Glaser, M. Semmling, K. Balidakis, J. Wickert, M. Maturilli, S. Dahlke, and H. Schuh, “GNSS-based water vapor estimation and validation during the MOSAiC expedition,” *Atmos. Meas. Tech.*, vol. 14, pp. 5127–5138, 2021.
- [20] ASSIST, “Arctic shipborne sea ice standardization tool,” International Arctic Research Center, <http://www.iarc.uaf.edu/icewatch>, Tech. Rep., 2016.
- [21] A. M. Semmling, J. Wickert, S. Schön, R. Stosius, T. Gerber, M. Markgraf, M. Ge, and G. Beyerle, “A zeppelin experiment to study airborne altimetry using specular Global Navigation Satellite System reflections,” *Radio Science*, vol. 48, pp. 427–440, 2013.

- [22] L. Peraza, A. M. Semmling, C. Falck, O. Pavlova, S. Gerland, and J. Wickert, “Analysis of Grazing GNSS Reflections Observed at the Zeppelin Mountain Station, Spitsbergen,” *Radio Science*, vol. 52, pp. 1352–1362, 2017.
- [23] A. M. Semmling, J. Beckheinrich, J. Wickert, G. Beyerle, S. Schön, F. Fabra, H. Pflug, K. He, J. Schwabe, and M. Scheinert, “Sea surface topography retrieved from GNSS reflectometry phase data of the GEOHALO flight mission,” *Geophysical Research Letters*, vol. 41, pp. 954–960, 2014.
- [24] K. M. Larson, E. E. Small, E. D. Gutmann, A. L. Bilich, P. Axelrad, and J. J. Braun, “Using GPS multipath to measure soil moisture fluctuations: initial results,” *GPS Solutions*, vol. 12, pp. 173–177, 2008.
- [25] A. M. Semmling, A. Rösel, D. Divine, S. Gerland, G. Stienne, S. Reboul, M. Ludwig, J. Wickert, and H. Schuh, “Sea Ice concentration derived from GNSS reflection measurements in Fram Strait,” *IEEE Trans. Geosci. Rem. Sens.*, vol. 57, no. 12, pp. 10 350–10 361, 2019.
- [26] M. Semmling, J. Wickert, S. Magnussen, T. Gerber, G. Spreen, L. Kaleschke, R. Ricker, and A. Tavri, “GNSS signal power data for reflectometry recorded during the MOSAiC Expedition (leg 1),” *GFZ Data Services*, 2021. [Online]. Available: <https://doi.org/10.5880/GFZ.1.1.2021.002>
- [27] N. Rodriguez-Alvarez, X. Bosch-Lluis, A. Camps, M. Vall-Ilossera, E. Valencia, J. F. Marchan-Hernandez, and I. Ramos-Perez, “Soil Moisture Retrieval Using GNSS-R Techniques: Experimental Results Over a Bare Soil Field,” *IEEE Trans. Geosci. Rem. Sens.*, vol. 47, pp. 3616–3624, 2009.
- [28] A. U. Schmitt and L. Kaleschke, “A Consistent Combination of Brightness Temperatures from SMOS and SMAP over Polar Oceans for Sea Ice Applications,” *Remote Sens.*, vol. 10, no. 553, 2018.
- [29] M. Leppäranta and T. Manninen, “The brine and gas contents of sea-ice with attention to low salinities and high temperatures,” *Technical Report 1988-2, Finnish Institute of Marine Research*, 1988.
- [30] M. Schwank, C. Mätzler, A. Wiesmann, U. Wegmüller, J. Pulliainen, J. Lemmetyinen, K. Rautiainen, C. Derksen, P. Toose, and M. Drusch, “Snow Density and Ground Permittivity Retrieved from L-Band Radiometry: A Synthetic Analysis,” *IEEE JSTARS*, vol. 8, pp. 3833–3845, 2015.
- [31] A. Egido, M. Caparrini, G. Ruffini, S. Paloscia, E. Santi, L. Guerriero, N. Pierdicca, and N. Floury, “Global Navigation Satellite Systems Reflectometry as a Remote Sensing Tool for Agriculture,” *Remote Sens.*, vol. 4, pp. 2356–2372, 2012.
- [32] V. U. Zavorotny, K. M. Larson, J. J. Braun, E. E. Small, E. D. Gutmann, and A. L. Bilich, “A Physical Model for GPS Multipath Caused by Land Reflections: Toward Bare Soil Moisture Retrievals,” *IEEE Journal of Selected Topics in Applied Earth Observations and Remote Sensing*, vol. 3(1), pp. 100–110, 2010.
- [33] P. Beckmann and A. Spizzichino, *The Scattering of Electromagnetic Waves from Rough Surfaces*. Nordwood, MA: Artech House, Inc., 1987, reprint. Originally published: Oxford [Oxfordshire]; New York : Pergamon Press, 1963. (International Series of Monographs on Electromagnetic Waves; 4).
- [34] E. Loria, A. O’Brien, V. Zavorotny, B. Downs, and C. Zuffada, “Analysis of scattering characteristics from inland bodies of water observed by CYGNSS,” *Remote Sensing of Environment*, vol. 245, 2020.



A. Maximilian Semmling graduated in physics from Leipzig University in 2007 and received the doctoral degree from Technische Universität Berlin in 2012. For his doctoral and post-doctoral studies, he was with the German Research Centre for Geosciences (GFZ), Germany, the Institute for Space Studies of Catalonia (IEEC), Spain, and the University of the Littoral Opal Coast (ULCO), France. In 2020 he joined the observation department at the German Aerospace Center (DLR), Institute for Solar-Terrestrial Physics.

He is experienced in GNSS for Earth Observation with research focus on ocean altimetry and sea ice remote sensing. Current work concentrates on influence of atmosphere and space weather. Corresponding methods cover a wide range of measurements from ground-based over maritime, airborne to satellite platforms.



Jens Wickert physicist, received the Ph.D. degree in geophysics/meteorology in 2002. He holds a joint professorship of GFZ with the Technische Universität Berlin on GNSS remote sensing, navigation and positioning. He is GFZ's research topic director "The Atmosphere in Global Change". Wickert has authored/co-authored over 260 ISI listed publications on GNSS Earth observation.



Frederik Kreß received a B.Sc. degree in geoinformatics from University of Augsburg and currently studies M.Sc. geodesy and geoinformation science at TU Berlin, where he carries out a Master Thesis in Global Navigation Satellite System reflectometry (GNSS-R) with the German Research Centre for Geosciences (GFZ), Potsdam. His research interests are remote sensing and geoinformation with focus on climatology and cryosphere.



Mohammed Mainul Hoque received his Bachelor in Electrical and Electronics Engineering in 2000 and was awarded a Ph.D. in 2009 from the University of Siegen, Germany. He has been working on ionospheric modeling, including higher order propagation effects at the German Aerospace Center (DLR) since 2004. Since 2019 he is the head of the Space Weather Observations department at the DLR Institute for Solar-Terrestrial Physics.



Dmitry V. Divine received the B.S. and M.S. degrees in physics and atmospheric physics from Saint-Petersburg State University, Saint Petersburg, Russia, in 1995 and 1998, respectively, and the Ph.D. degree in physical oceanography from the University of Bergen, Norway, in 2003. He was a Post-Doctoral Fellow with the Norwegian Polar Institute, Tromsø, Norway, and the University of Tromsø, The Arctic University of Norway, Tromsø, from 2003 to 2012. He is currently a Senior Research Scientist in sea ice physics and paleoclimate with the Norwegian Polar Institute. His research interests include sea-ice remote sensing, study of snow and sea ice mass balance from in situ and airborne observations, application of photogrammetry from low-altitude airborne imagery to study sea-ice processes at the broad range of spatial scales.



Sebastian Gerland received the master's (Dipl. Geophys.) degree in geophysics from Johann Wolfgang Goethe University, Frankfurt, Germany, in 1989, and the Ph.D. (Dr. rer. nat.) degree in marine sediment physics from the University of Bremen, Germany, in 1993. He was with Glaciology Groups at the Alfred Wegener Institute, Bremerhaven, Germany, and the University College of London, U.K., and worked with radioecology at the Norwegian Radiation Protection Authority in Tromsø, Norway. From 1997 to 2000 and since 2002, he has been with the Norwegian Polar Institute, Tromsø, Norway, where he is currently a Senior Research Scientist for sea ice and climate as well as head of the section "Oceans and Sea Ice." His research interests include sea-ice mass and energy balance in the Arctic, with a focus on the regions Fram Strait, Barents Sea, Svalbard, and Arctic Basin.



Gunnar Spreen (M'08) received his M.Sc. degree in physics (Diplomphysiker) in 2004 and the Ph.D. degree in oceanography in 2008, both from the University of Hamburg, Germany. He works on satellite remote sensing of Polar Regions with focus on monitoring changes of sea ice (extent, mass, and dynamics) and on understanding underlying climate processes. Satellite measurements are validated using ground-based and airborne field observations, recently in particular from the 2019/2020 MOSAiC expedition. For which he serves on the Project Board and coordinates the remote sensing activities. Gunnar Spreen is the head of the research group "Remote Sensing of Polar Regions" at the University of Bremen, Institute of Environmental Physics, Bremen, Germany. Before, he was a research scientist at the Norwegian Polar Institute, Tromsø, Norway and a postdoctoral scholar at the Jet Propulsion Laboratory, California Institute of Technology, Pasadena, CA, USA. Current work addresses the development of new retrievals for sea ice parameters like leads and ice type from SAR and microwave radiometer data as well as snow on sea ice.

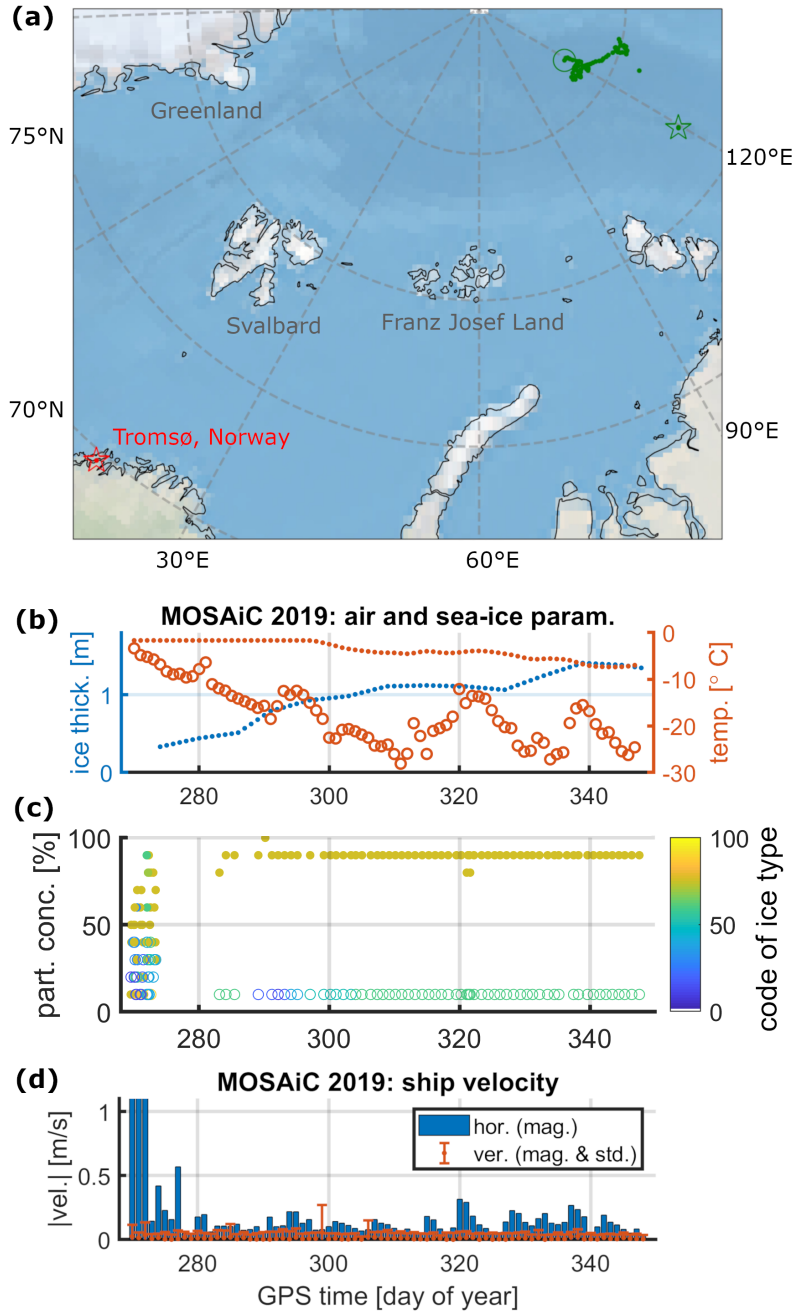


Fig. 1. **Panel (a):** Map indicating the ship's location for the analyzed measurements (green markers). First and last day are indicated by a green star and circle, respectively. Data from the transit period between the start of the expedition in Tromsø (red star) and the start of the analyzed measurements (green star) cannot be used for publication due to restrictions in the exclusive economical zone of Norway and Russia. **Panel (b):** ancillary data of daily averaged 2-m air temperature (open red circles) and sea-ice temperature at bottom layer (red dots) as well as sea-ice thickness data (blue dots). **Panel (c):** visual on-board observations indicating partial sea-ice concentration of primary and secondary ice type (filled and open markers). Color-coding classifies the ice type on a scale increasing with age: second-year ice (75) is most often primary type, first-year ice (60) is most often secondary type, early in the shown period also younger ice (50 and below) is reported with thickness < 30 cm. **Panel (d):** ship's velocity data from GNSS: daily mean values of horizontal velocity (blue bars) and vertical velocity (red dots), error bars indicate daily standard deviation.

October 19, 2021

DRAFT

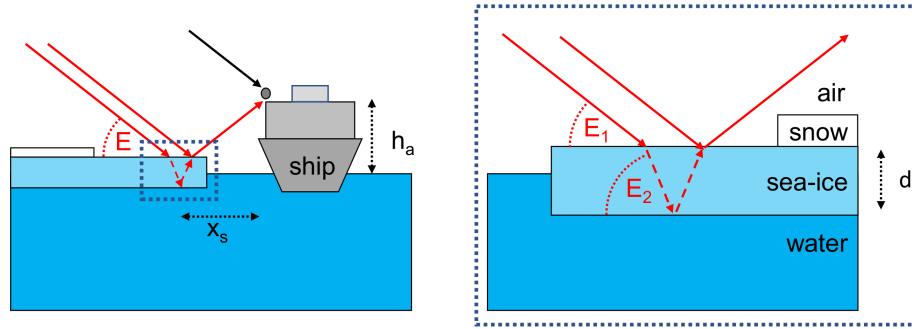


Fig. 2. **Left panel:** Concept of ship-based reflectometry observations over a sea-ice covered surface, antenna height level h_a relative to the surface, elevation angle E at the surface reflection point, distance x_s of reflection point from setup. **Right panel:** Zoom into a sea-ice slab reflection considering contribution from air-ice and ice-water interface, slab thickness d , elevation angles E_1 and E_2 at the respective interfaces.

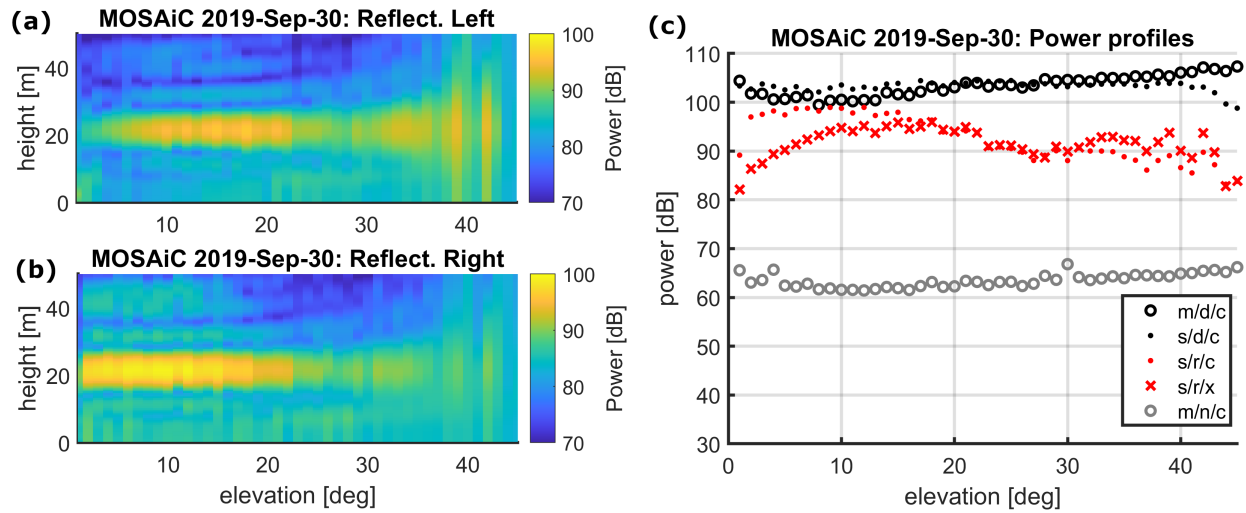


Fig. 3. **Panels (a) and (b):** Height-elevation maps of LHCP slave link (a) and RHCP slave link (b) with sea-surface reflection signatures at about 21 m. **Panel (c):** Estimated power profiles over elevation angle, coded according to: master/slave link (m,s), direct/reflected signal/noise (d,r,n) and co-/cross-polar link polarization (c,x). Power estimates are based on the sum of post-correlation counts.

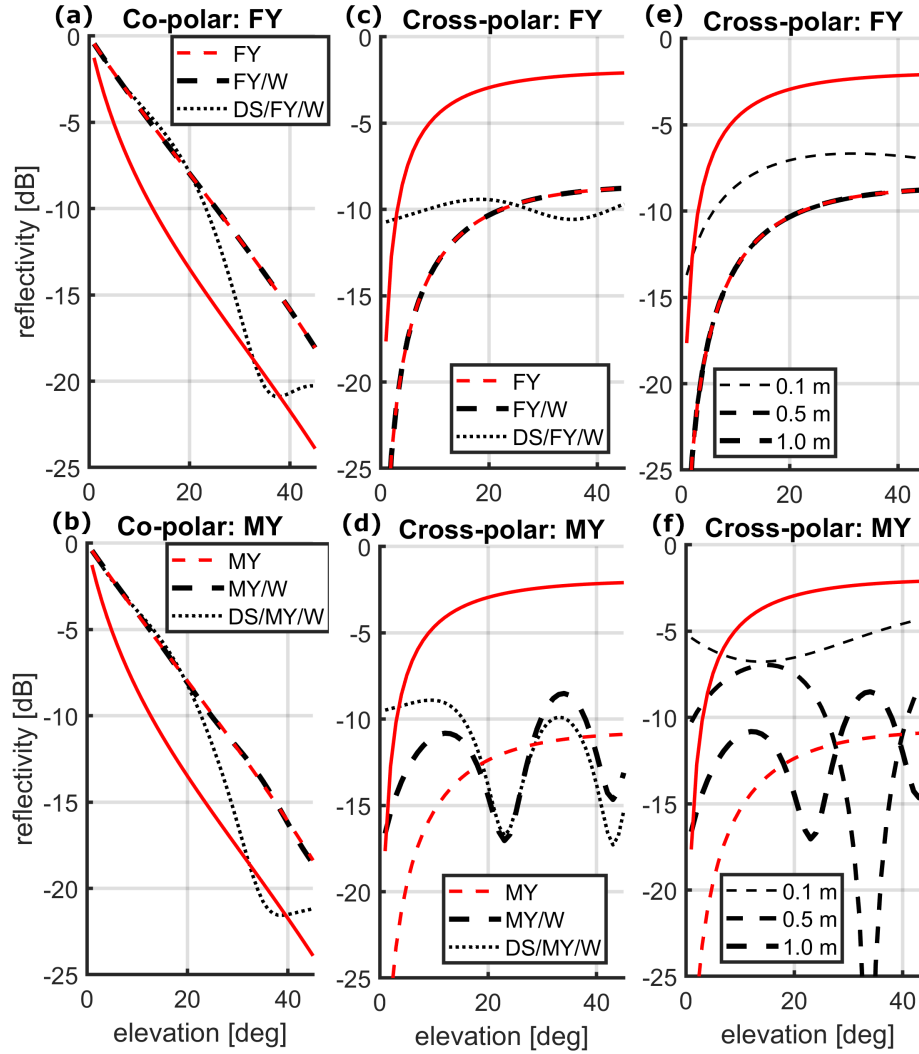


Fig. 4. Model predictions of reflectivity, **panels (a) and (b)** show co-polar and **panels (c) to (f)** cross-polar profiles. Different ice types are considered: first-year (FY) ice in upper panels and multiyear (MY) ice in the lower panels. Red curves refer to reflectivity of a bulk medium: water (solid line), ice (dashed line). Black curves, in general, refer to reflectivity in a slab configuration: ice over water (FY/W or MY/W) given by dashed lines, dry snow over ice and water (DS/FY/W or DS/MY/W) given by dotted lines. Considered relative permittivity agrees with Tab. I. In the panels **(a),(b)** and **(c),(d)** slab thickness is set to 1 m for ice and 20 cm for snow. In the panels **(e),(f)** the ice slab thickness varies among the black curves between 0.1 m and 1.0 m, snow is not considered there.

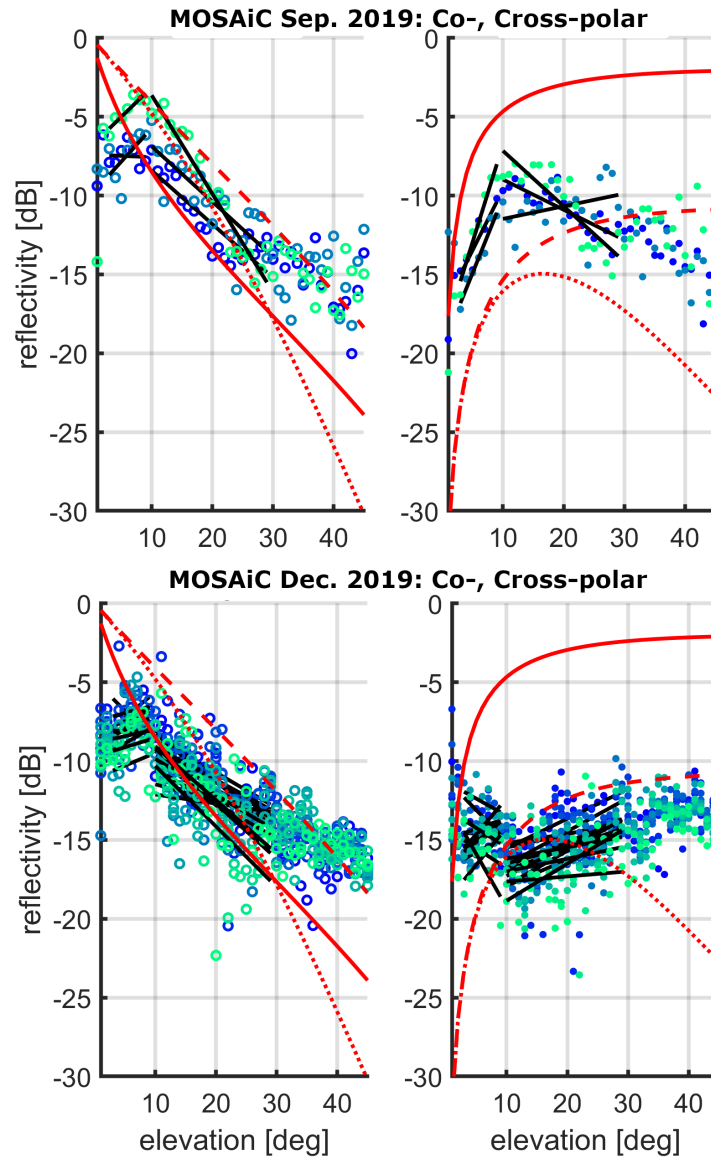


Fig. 5. Reflectivity profiles over elevation angle retrieved from co- and cross-polar observations. Upper plots: three days of late transit period in Sep-2019 (DoY 271-273). Lower plots: last two week of the in-ice period during leg-1 in Dec-2019 (DoY 335-348). The profiles in each plot are color-coded: earlier days (blue), later (green). Bulk model predictions are added: sea water (solid red), smooth MY ice (dashed red) and rougher type of MY ice (dotted red) assuming 10-cm surface height standard deviation. Fitting lines (black) for each daily profile are shown separately for low- and mid-elevation range: 3° to 10° and 10° to 30° , respectively.

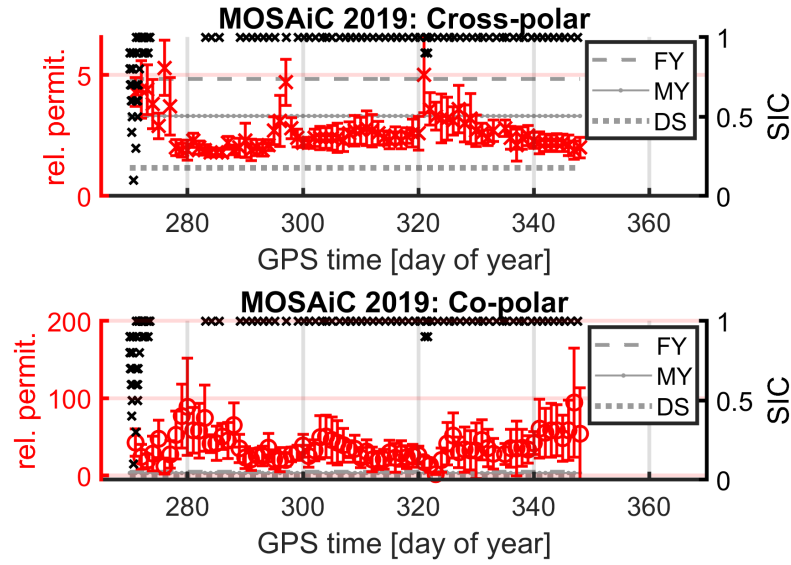


Fig. 6. Relative permittivity inverted from cross- and co-polar reflectivity profiles over day of year using all available data (DoY 271 to 348 in 2019). Values of relevant media: FY ice, MY ice and DS, are shown as respective gray lines for comparison. Total SIC (black marker, right axis) has an influence on permittivity.

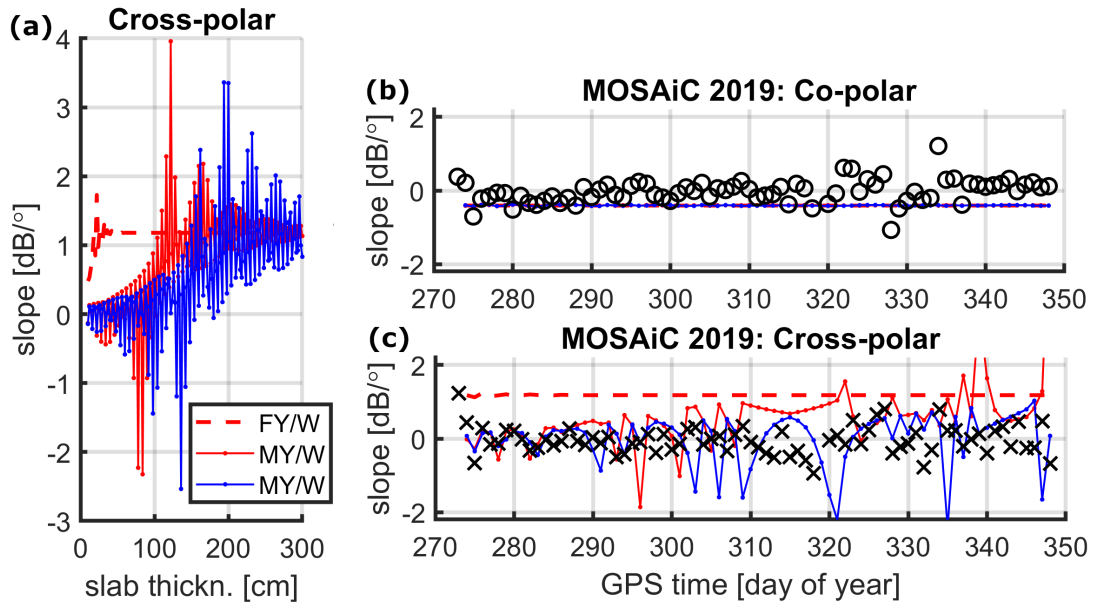


Fig. 7. **Panel (a):** model prediction of slope m_{low} over slab thickness for different slab configurations on underlying water (W): FY slab at -1°C (red dashed curve), MY slab at -1°C (red dotted curve) and MY slab at -10°C (blue dotted curve). **Panel (b),(c):** retrievals of slope m_{low} for co- and cross-polar data, respectively, during in-ice period with respective prediction curves added.

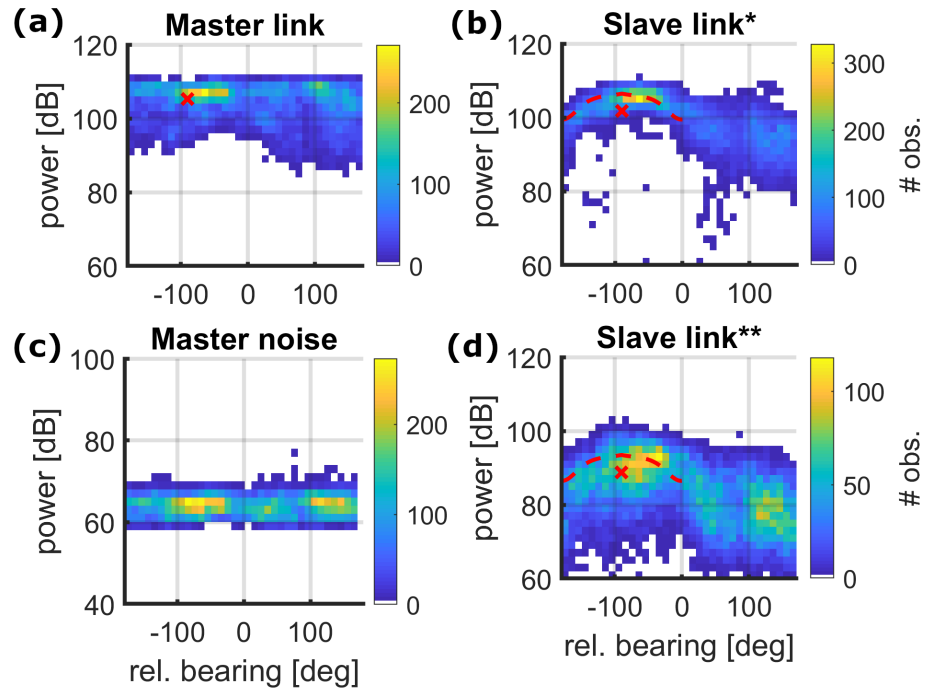


Fig. 8. Power estimate distribution over relative bearing based on December data (DoY 335 to 348). **Panels:** direct signal on master link (a), direct signal on RHCP slave link (b), noise level on master link (c) and reflected signal on LHCP slave link (d). The master link refers to the up-looking, the slave links to the port-side-looking antenna. Red crosses show power level after stacking all observations, the respective bearing is set to the boresight direction of slave antenna (-90°). For slave links (b) and (d) the gain pattern variation relative to boresight is added above the stack result (dashed line).